

PSP/IS \odot IS observations of the 29 November 2020 solar energetic particle event[★]

C. M. S. Cohen¹, E. R. Christian², A. C. Cummings¹, A. J. Davis¹, M. I. Desai³, G. A. de Nolfo², J. Giacalone⁴, M. E. Hill⁵, C. J. Joyce⁶, A. W. Labrador¹, R. A. Leske¹, W. H. Matthaeus⁷, D. J. McComas⁶, R. L. McNutt Jr.⁵, R. A. Mewaldt¹, D. G. Mitchell⁵, J. G. Mitchell^{2,8}, J. S. Rankin⁶, E. C. Roelof⁵, N. A. Schwadron⁹, E. C. Stone¹, J. R. Szalay⁶, M. E. Wiedenbeck¹⁰, A. Vourlidas⁵, S. D. Bale^{11,12}, M. Pulupa¹², and R. J. MacDowall²

¹ California Institute of Technology, Pasadena, CA 91125, USA
e-mail: cohen@srl.caltech.edu

² NASA/Goddard Space Flight Center, Greenbelt, MD 20771, USA

³ University of Texas at San Antonio, San Antonio, TX 78249, USA

⁴ University of Arizona, Tucson, AZ 85721, USA

⁵ Johns Hopkins University Applied Physics Laboratory, Laurel, MD 20723, USA

⁶ Department of Astrophysical Sciences, Princeton University, Princeton, NJ 08544, USA

⁷ University of Delaware, Newark, DE 19716, USA

⁸ Department of Physics, George Washington University, Washington, DC 20052, USA

⁹ University of New Hampshire, Durham, NH 03824, USA

¹⁰ Jet Propulsion Laboratory, California Institute of Technology, Pasadena, CA 91109, USA

¹¹ Physics Department, University of California at Berkeley, Berkeley, CA 94720, USA

¹² Space Sciences Laboratory, University of California at Berkeley, Berkeley, CA 94720, USA

Received 31 March 2021 / Accepted 23 August 2021

ABSTRACT

Aims. On 29 November 2020, at 12:34 UT, active region 12790 erupted with an M4.4 class flare and a 1700 km s^{-1} coronal mass ejection. Parker Solar Probe (PSP) was completing its seventh orbit around the Sun and was located at 0.8 au when the Integrated Science Investigation of the Sun (IS \odot IS) measured the ensuing mid-sized solar energetic particle (SEP) event. Not only was this the first SEP event with heavy ions above 10 MeV nuc^{-1} to be measured by IS \odot IS, it was also measured by several spacecraft positioned around the Sun, making it the first circumsolar event of solar cycle 25. Here we describe an overview of the SEP event characteristics at PSP.

Methods. Fluence spectra for electrons, H, He, O, and Fe were calculated for the decay portion of the event. For the entire time period of the event, it was possible to calculate fluence spectra for electrons, O, and Fe only due to instrumental mode changes in one of the IS \odot IS telescopes, affecting H and He during the period of peak intensities. Using higher time resolution data, we also studied the onset of the event and temporal variations in the particle intensities at the shock and during the magnetic cloud passage.

Results. During the decay, the ion spectra are consistent with power laws at low energies with an exponential rollover at a few MeV nuc^{-1} , while the electron spectrum is consistent with a power law of index -5.3 . Based on fits to the spectra, Fe/O and He/H abundance ratios as a function of energy are calculated and found to be nominal for large SEP events at hundreds of keV/nuc, but decrease strongly with increasing energy. The full-event spectra for O and Fe have similar shapes to those of the decay, but with higher roll-over energies. The electron spectrum for the full event is harder with an index of -3.4 and there is some evidence of higher energy components near $\sim 2 \text{ MeV}$ and above $\sim 4 \text{ MeV}$. Despite the spacecraft being tilted 45° with respect to the nominal orientation of the spacecraft's long axis pointed towards the Sun, there is some anisotropy apparent in MeV protons during the onset of the event. Velocity dispersion is also evident, consistent with a solar release time of 13:15 UT and pathlength of 1.3 au. The arrival of the related magnetic cloud resulted in the suppression of SEP intensities, although a brief increase in particle intensities suggests PSP moved out of the cloud for $\sim 30 \text{ min}$. This appears to be the first medium-sized event in the rise of cycle 25 activity, with additional large events likely to occur. Additional details of the event beyond this overview can be found in several related papers.

Key words. Sun: particle emission – Sun: activity – solar-terrestrial relations

1. Introduction

The Parker Solar Probe (PSP, Fox et al. 2016) mission is designed to examine the solar wind and energetic particles at distances closer to the Sun than previous missions with three in situ instrument suites: Electromagnetic Fields Investigation (FIELDS, Bale et al. 2016), Solar Wind Electron Alpha Proton (SWEAP, Kasper et al. 2016), and Integrated Science

Investigation of the Sun (IS \odot IS, McComas et al. 2016). Through a series of Venus flybys, the perihelion of the PSP orbit will be reduced to $< 10 R_\odot$ by the end of 2024. As of March 9, 2021, PSP has completed seven orbits, with a closest approach of $20.4 R_\odot$ on January 17, 2021. During these seven orbits, the solar activity has been very low, resulting in IS \odot IS observing only a few small solar energetic particle (SEP) events until late November 2020.

These SEP events have been described in detail in a number of papers (McComas et al. 2019; Cohen et al. 2021; Giacalone et al. 2020; Hill et al. 2020; Joyce et al. 2021;

* Movie associated to Fig. 2 is available at <https://www.aanda.org>

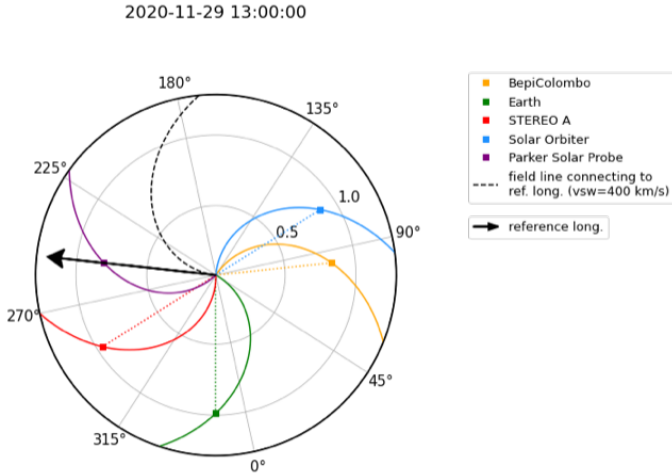


Fig. 1. Relative positions of various spacecraft on 29 November 2020 at 13:00 UT as viewed from above the ecliptic plane. Nominal Parker spirals are shown for each spacecraft position assuming a solar wind speed of 400 km s^{-1} . The Carrington longitude of the solar source region is indicated by the black arrow.

(Leske et al. 2020; Mitchell et al. 2020; Schwadron et al. 2020; Wiedenbeck et al. 2020). Due to low particle intensities in these events, the analysis has been limited to observations of protons and helium, generally at energies $\leq 10 \text{ MeV nuc}^{-1}$, and electrons below a few MeV. An additional consequence of the small size of the events is that it has not been possible to fully calibrate the energetic particle instruments, particularly their response to heavy ions (i.e., $Z > 2$). This changed on 29 November 2020 when IS \odot IS observed a mid-sized SEP event, with heavy-ion intensities observed at tens of MeV nuc^{-1} and a 0.3 MeV nuc^{-1} He fluence of $3.9 \times 10^7 (\text{cm}^2 \text{ sr MeV nuc}^{-1})^{-1}$ (putting it close to the mean fluence of a survey of multi-spacecraft events by Cohen et al. 2017).

The characteristics of the related solar eruption and coronal mass ejection (CME) are briefly described below. The resulting SEP event was observed by multiple spacecraft positioned around the Sun, including the recently launched Solar Orbiter spacecraft (SolO, Müller et al. 2020). The relative positions of PSP, STEREO, SolO, and near-Earth spacecraft, such as ACE, Wind, and SOHO, are given in Fig. 1. The multi-spacecraft aspects of this SEP event are described in Kollhoff et al. (2021). In this paper we concentrate on the measurements made by IS \odot IS, providing a general overview of the energetic particle observations.

2. Solar source and activity

On November 29 (day 334), 2020, active region 12790 was just behind the east limb of the Sun as observed by Earth. The GOES-16 X-ray instrument reported an M4.4 class flare starting at 12:34 UT, peaking at 13:11 UT and ending at 13:34 UT. The flare location was 99°E and 23°S relative to the Earth's central meridian, putting it just 2°E of PSP and 51°E of STEREO-A, and allowing STEREO-A a clear view of the eruption. The outward evolution of the CME is best seen from the SDO/AIA perspective (Fig. 2 and accompanying movie). The early signs of a hot flux rope can be discerned in the 131 \AA channel from about 12:33 UT onwards. A clear flux rope appears by 12:47 UT and the event acquires typical CME signatures from then on (expanding extreme ultraviolet (EUV) bubble and post-CME loops).

The EUV bubble leaves the AIA field-of-view, while a southward expansion of the eruption becomes apparent in the EUVI-A and AIA 304 \AA images. A relatively dark filament can be seen propagating southward and lifting off the surface by 13:08 UT. Our height-time measurements of the CME front in the LASCO field-of-view indicate that the CME entered the LASCO C2 field-of-view with a speed of $\sim 1900 \text{ km s}^{-1}$ and decelerated to 1500 km s^{-1} by $25 R_\odot$ (Fig. 3). The event was certainly capable of driving a shock in the corona. As the active region was close to the solar limb as viewed by SOHO, the projection effects are minimal, leading to a good estimate of the CME speed. Figure 4 shows combined STEREO-A/EUVI and SDO/AIA observations of the active region and the CME as observed by SOHO/LASCO but projected to be consistent with a view from STEREO-A. The estimated PSP magnetic footprint was located about 70° westward from the flare site (determined from ENLIL simulations, L. Rodriguez-Garcia, priv. comm., and marked by the star in Fig. 4). The inset STEREO-A/COR2 white light image of the CME shows the spatial extent of the structure, including towards the west where the nominal magnetic footprint of PSP was located.

The “bend” in the region under the flare loops is the location of the start of the flare (see expanded view in the lower-right of Fig. 4 and marked by the location label ‘99E 23S’). Such curved polarity inversion lines (PILs) are often associated with strong CME and flare events. For example, the CMEs on July 19, 2012 (Patsourakos et al. 2013) and September 6–10, 2017 (Sun & Norton 2017) were associated with similarly bent PILs. It is most likely a signature of strong shear, probably due to a rotating sunspot. Although the November 29 SEP event was not as large as those associated with the July 2012 and September 2017 events, it was significant. Of particular interest is the fact that this SEP event was observed not only by STEREO-A and PSP (both of which were in the path of the CME), but also by SOHO, ACE, and Wind at L1 and SolO which were substantially west and east of the source region, respectively. This suggests that interplanetary conditions were conducive to a rapid spread of energetic particles in longitude. Details regarding this, as well as the magnetic connectivity between the spacecraft and the flare and CME, can be found in Kollhoff et al. (2021).

Prior to the event CME, there was a slower ($\sim 524 \text{ km s}^{-1}$ Nieves-Chinchilla et al. 2021) CME launched in association with a C2.6 flare from active region 12787 (N30E89) at 19:20 UT on November 26. While this event is not particularly noteworthy in itself, its trajectory was such that it also passed over PSP. Due to the relative timing and speeds of the two CMEs, their interaction (with the November 29 CME overtaking the November 26 CME) occurred approximately at the location of PSP. This is discussed more in Sect. 6 as well as in Nieves-Chinchilla et al. (2021) and Lario et al. (2021).

3. Instrumentation

Together, Energetic Particle Instrument-Low and -High (EPI-Lo and EPI-Hi, respectively) of IS \odot IS enable energetic ions to be measured from $\sim 20 \text{ keV}$ to $> 100 \text{ MeV nuc}^{-1}$ and energetic electrons from $\sim 15 \text{ keV}$ to $\sim 6 \text{ MeV}$. As described in McComas et al. (2016) and Hill et al. (2017), EPI-Lo is a time-of-flight versus energy instrument with 80 separate apertures distributed between 8 sectors resulting in a $2\pi\text{-sr}$ field of view. EPI-Hi (McComas et al. 2016; Wiedenbeck et al. 2017) is a set of three telescopes of stacked silicon detectors, using the standard dE/dx versus residual energy measurement technique. One of the Low Energy Telescopes (LETs) is double-ended, with

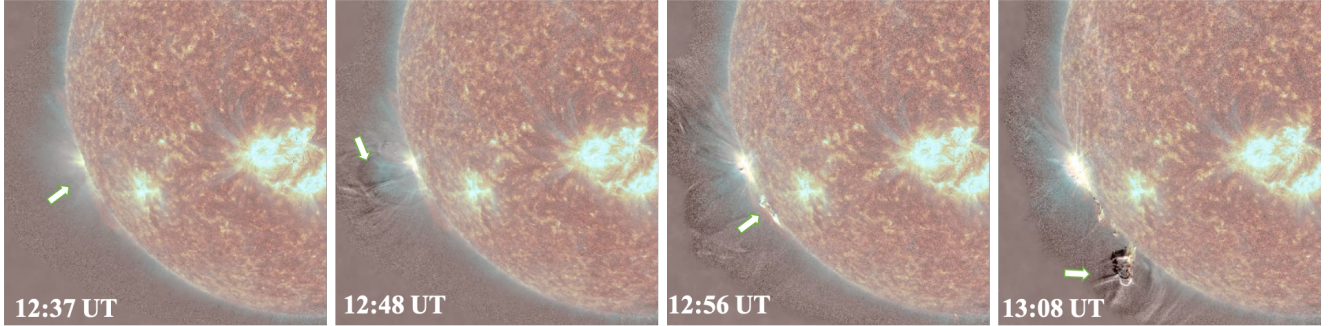


Fig. 2. Snapshots of the CME early evolution as seen in AIA 131 Å (blue hues), 304 Å (red image) and 195 Å (running difference; black and white) channels. The arrows point to features discussed in the corresponding text (two left frames: formation of hot flux rope; two right frames: southern expansion and eruption of a filament). These constitute the two components of the CME detected in the coronagraphs. The full animation is available [online](#).

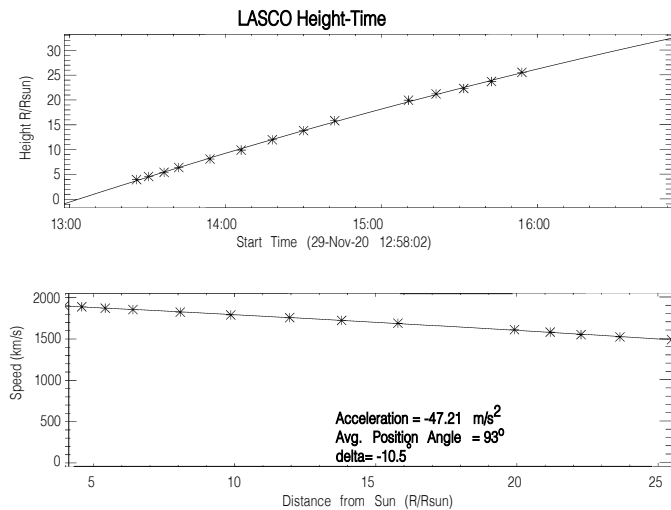


Fig. 3. CME kinematics as measured in the LASCO field of view. The height-time profiles correspond to the fastest propagating point along the CME front.

apertures named LETA and LETB. The other LET is single ended, with its aperture designated LETC. The third telescope is the High Energy Telescope (HET), also double-ended with apertures HETA and HETB. LETA is mounted with its axis 45° relative to the spacecraft's long axis, or Z axis, (i.e., along the nominal Parker spiral at 1 au when the spacecraft's Z-axis is pointed towards the Sun); LETC is mounted orthogonal to the axis of LETA. The axis of HETA is 20° relative to the spacecraft's Z axis. All the telescope axes lie in the orbital plane (approximately the ecliptic plane).

At the time of the November event, PSP was at ~ 0.8 au from the Sun. Due to communication requirements, the spacecraft was tilted such that its Z axis was pointed 45° westward from the Sun. This orientation resulted in LETA pointing 90° from the Sun, or approximately along the +T direction in RTN coordinates (where R is radially outward from the Sun, and along the spacecraft $-Z$ axis during encounters, T is the cross product of the solar rotation axis and R and N completes the righthanded coordinate system). Additionally, at various times during the event, the spacecraft was also rolled 180° about the spacecraft-sun line, resulting in LETA being aimed along the $-T$ direction. Such changes need to be noted when interpreting any differences in the intensities measured by LETA versus LETB or HETA versus HETB (as is done in Sect. 6).

The SEP event had proton intensities sufficiently high to trigger EPI-Hi to activate its dynamic threshold system. Normal operation is considered dynamic threshold mode (DT) 0 and during the event the telescopes entered DT 1, 2, and for LETA and LETB, 3. Modes 1–3 involve increasing the energy threshold of certain detector segments in order to decrease the instrument's response to protons, helium, and electrons. This allows the instrument livetime to remain relatively high and prioritize the heavy ion ($Z > 2$) measurements. The segments with threshold changes for each dynamic threshold mode are listed in Table 1, illustrated in Fig. 5, and discussed in more detail in Wiedenbeck et al. (in prep.). The trigger for the instrument entering dynamic thresholds is the counting rate measured by the front-end electronics exceeding a set value; this value is a commandable parameter which is set at a level that corresponds to when the instrument dead-time is considered excessive. Although some testing of the dynamic threshold modes was performed before launch, this is the first time EPI-Hi has exercised these modes in flight. Although LETA and LETB performed in DT1 as expected, they did not in DT2 as a parameter in the instrumental logic for DT2 was not appropriately initialized. Unfortunately, this led to a substantial loss of H and He statistics from LETA and LETB while in DT2 (November 30 (day 335), 15:00 UT – December 1 (day 336), 03:00 UT) as can be seen in Fig. 6. This initialization has subsequently been corrected and will allow proper functionality of DT2 in future large events.

For context, in addition to the FIELDS (Bale et al. 2016) magnetometer data, we use the radio observations from the FIELDS Radio Frequency Spectrometer (RFS, Pulupa et al. 2017). The arrival of the November 26 CME is evident in the magnetometer data as a small interplanetary shock (late on November 29, day 334) and a magnetic cloud (early November 30, day 335). This is followed by the strong shock, sheath, and magnetic cloud associated with the fast November 29 CME. Details regarding these structures are discussed more in Sect. 6. The radio data reveal several type III bursts and a type II burst associated with the event flare and CME, respectively. Unfortunately, due to the spacecraft tilt, the solar wind data from SWEAP are only available for the start of the event and do not provide information about the shock, sheath or cloud periods and are not used in this study.

4. SEP event overview

An overview of the event as measured by IS \odot IS is illustrated in Fig. 6. Shown in panels a–c are spectrograms of H from HETA,

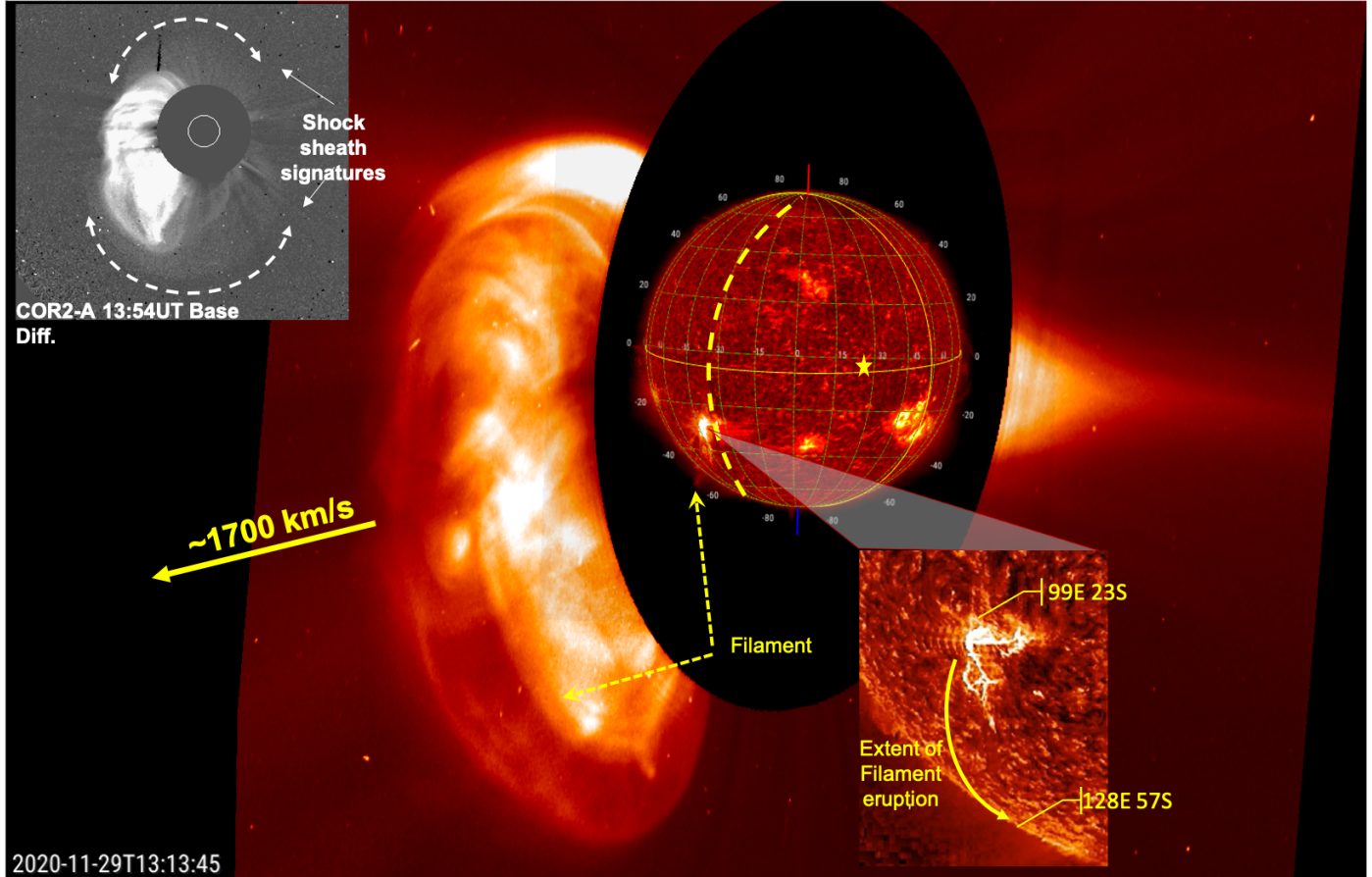


Fig. 4. Overview of the erupting filament and corresponding CME from the STEREO-A point of view. The inner solar image is a composite of SDO/AIA and STEREO-A/EUVI 304 Å, with the east limb as viewed from Earth indicated by the dashed yellow arc. The location of the estimated PSP magnetic footprint is marked by the yellow star. The bottom-right insert shows a closer view of the active region where the ‘bend’ in the bright structure at 99E 23S is the origin of the flare. The curved yellow arrow illustrates the extent of the filament eruption, primarily southward to 128E 56S (all locations are relative to the Earth central meridian at that time). The CME image is from LASCO and rotated to correspond to the STEREO-A point of view; the upper-left insert shows the CME as measured by STEREO-A/COR2 for comparison. The CME traveled largely in the plane of the sky as viewed by LASCO, thus projection effects are minimal on the derived velocity of $\sim 1700 \text{ km s}^{-1}$. The figure was made with the help of the Jhelioviewer software tool (Müller et al. 2017).

Table 1. Dynamic threshold modes.

Threshold mode	LETA/B segments with raised thresholds	LETc segments with raised thresholds	HET segments with raised thresholds
0	No segments	No segments	No segments
1	L0 all segments L1 outer segments	L0 all segments L1 outer segments	H1 outer segments H2 outer segments
2	L0 all segments L1 all segments L2A outer segments L2B all segments L3B, L4B	L0 all segments L1 all segments L2 outer segments L5, L6	H1 all segments H2 all segments H3 all segments
3	All detectors, except pixel	All detectors, except pixel	All detectors, except pixel

LETA, and EPI-Lo (averaged over all the apertures except for 31, which has a high rate of photon-induced accidents due to a light leak resulting from a puncture in its foil window by a dust particle Hill et al. 2020). Panels d and e present He and electrons from HETA and the radio data are in panels f and g showing the type III and type II radio bursts (see also Fig. 13). The magnetic

field data are in the bottom panel h with vertical lines indicating the times at which the interplanetary shocks and magnetic clouds pass the spacecraft (see Sect. 6). Although the decay of the event continues past December 4 (day 339), ISOIS begins to experience significant data gaps due to the instrument being turned off while the spacecraft is using its *Ka*-band antenna; thus we

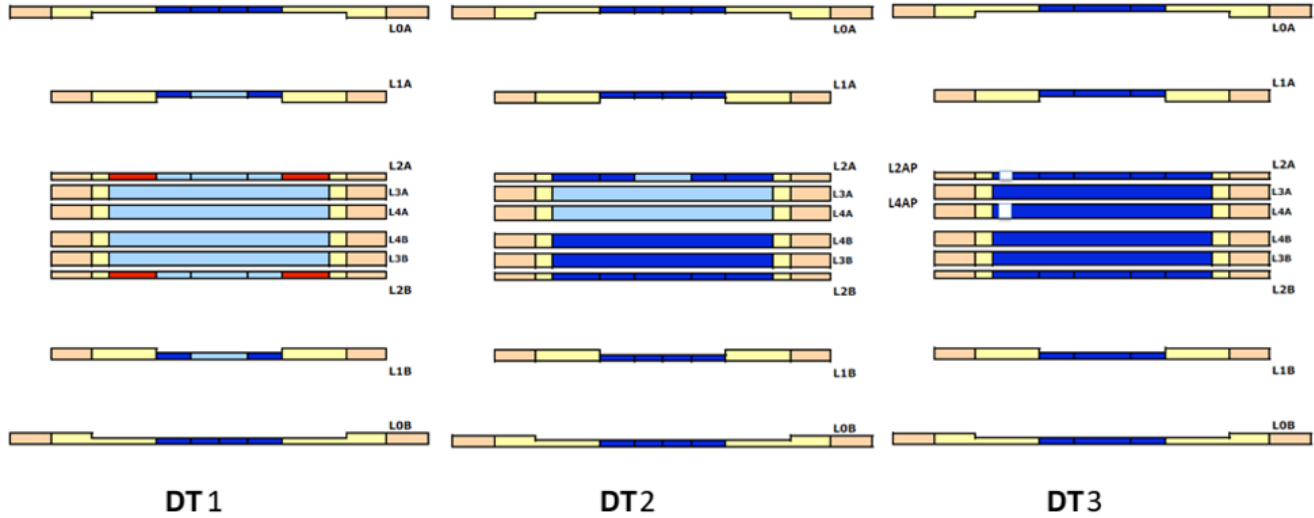


Fig. 5. Schematics of the detectors comprising the LETA+LETB telescope (shown as a cross-section of circular detectors). Beige portions correspond to the detector mountings, yellow portions indicate inactive silicon, and red sections are detector guard rings. Segments are colored dark blue to indicate their thresholds are raised in each of the dynamic threshold modes (1, 2, and 3, *left to right*, respectively). The white squares shown on the L2A and L4A detectors in mode 3 are ‘pixel’ segments.

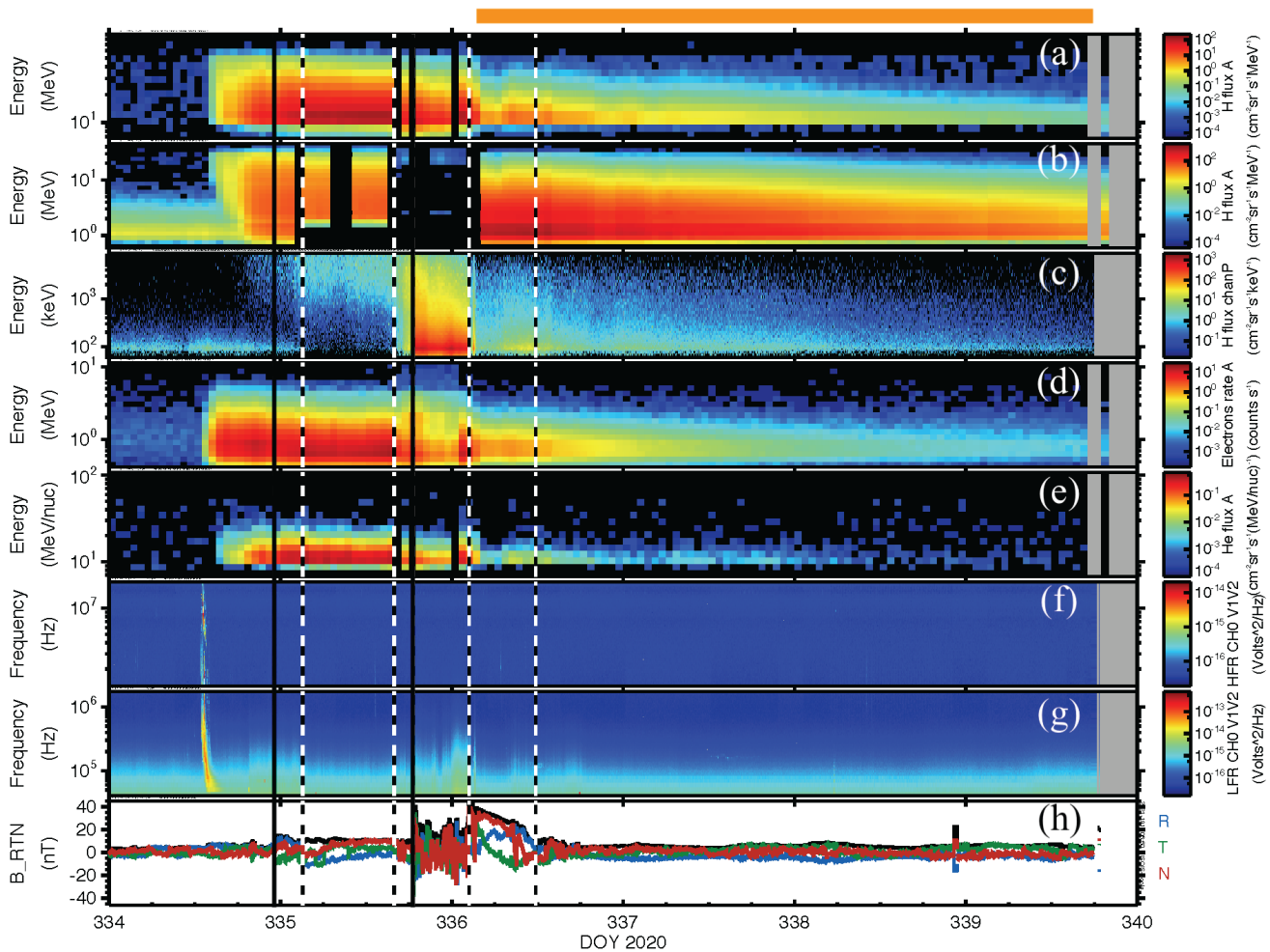


Fig. 6. Overview of the SEP event; panels *a–c* are protons from HETA, LETA, and EPI-Lo (respectively). Panels *d* and *e*: electron rate and He intensities from HETA. Panels *f* and *g*: high and low frequency radio observations and panel *h*: magnetic field magnitude (black line) and RTN components. The times of the shock passages are marked by the solid vertical lines and the periods of the magnetic clouds are bounded by the pairs of dashed vertical lines. The horizontal orange bar at the top indicates the integration period for the decay spectra. See text for further explanation of the instrumental effects apparent in panel *b*.

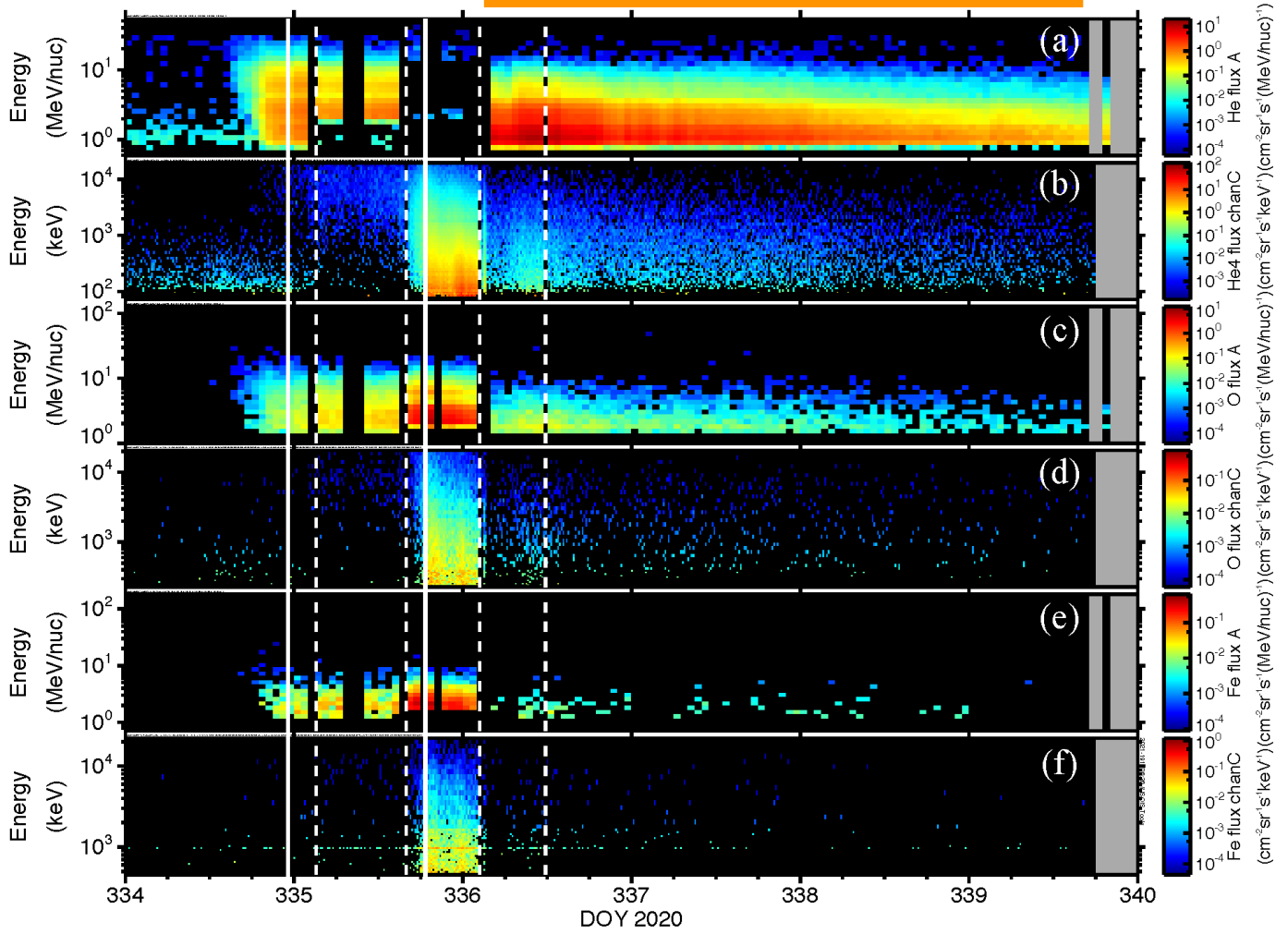


Fig. 7. Heavy ion spectrograms for the event in LETA/EPI-Lo panel pairs (*upper* and *lower* panels, respectively). Panels *a* and *b*: He intensities; *c* and *d*: oxygen intensities; and *e* and *f*: iron. See text for further explanation of the instrumental effects apparent in panel *a*. Solid vertical lines mark the passages of shocks and pairs of dashed lines indicate the magnetic cloud periods. The horizontal orange bar at the top indicates the integration period for the decay spectra.

concentrate on the time period from event onset on November 29 (day 334), ~12:00 UT to start of the first data gap on December 4 (day 339), 17:00 UT. The additional data gaps (identified as black bands in the plot) in the HETA and LETA data are due to hours in which EPI-Hi was changing dynamic threshold modes. The effects of DT1 in the increase of the lower energy threshold on H and He can be seen in panel *b* of Fig. 6 and panel *a* of Fig. 7, respectively, from November 30 (day 335), 03:00 UT to 15:00 UT. The decay portion of the event (December 1 (day 336), 04:00 UT – December 4 (day 339), 17:00 UT as indicated by the orange bar at the top of the plot) is particularly suitable for analysis as EPI-Hi was in its nominal configuration and there were no data gaps. The combined IS \odot IS fluence spectra for H, He, O and Fe for this period are discussed in the next section.

HET also exercised dynamic thresholds but primarily DT1 (with only a brief excursion into DT2 on November 30 (day 335), 18:33 UT to 18:37 UT). The set of detector segments selected for increased thresholds for HET is different from that of LET in DT1 such that the main effect is a reduction in the geometry factors. Simple corrections to apply the reduced geometry factors rather than the default values have been made to the HET H and electron data; this allows the temporal evolution of

the full event to be studied along with measurements made by EPI-Lo (see Sect. 6). It should be noted that as this is the first time in the mission HET has utilized DT1 (or higher), such corrections have not been required in past SEP events and are still being refined.

The November 29 SEP event was the first event large enough for heavy ions to be measured by IS \odot IS up to energies of tens of MeV nuc $^{-1}$. Heavy ion spectrograms for the event are given in Fig. 7 for LETA and EPI-Lo. Although the event intensities increased by several orders of magnitude, ions heavier than He were not measured by HET, suggesting that the intensities decreased substantially with increasing energy above ~10 MeV nuc $^{-1}$. This is verified by the spectra and their fits and is discussed more in the next section. The lesser impact of the dynamic thresholds on LETA's measurements of ions heavier than He is apparent in Fig. 7. Thus, O and Fe fluence spectra from EPI-Lo, LETA and LETB can be calculated for the entire event.

The temporal evolution of the lower energy ions (e.g., below ~1 MeV) is clearly different than that of the higher energy ions, as evidenced by the striking increase in intensities measured by EPI-Lo on November 30 (day 335), 18:35 UT, corresponding to the arrival of the second shock (see also Fig. 12). Although

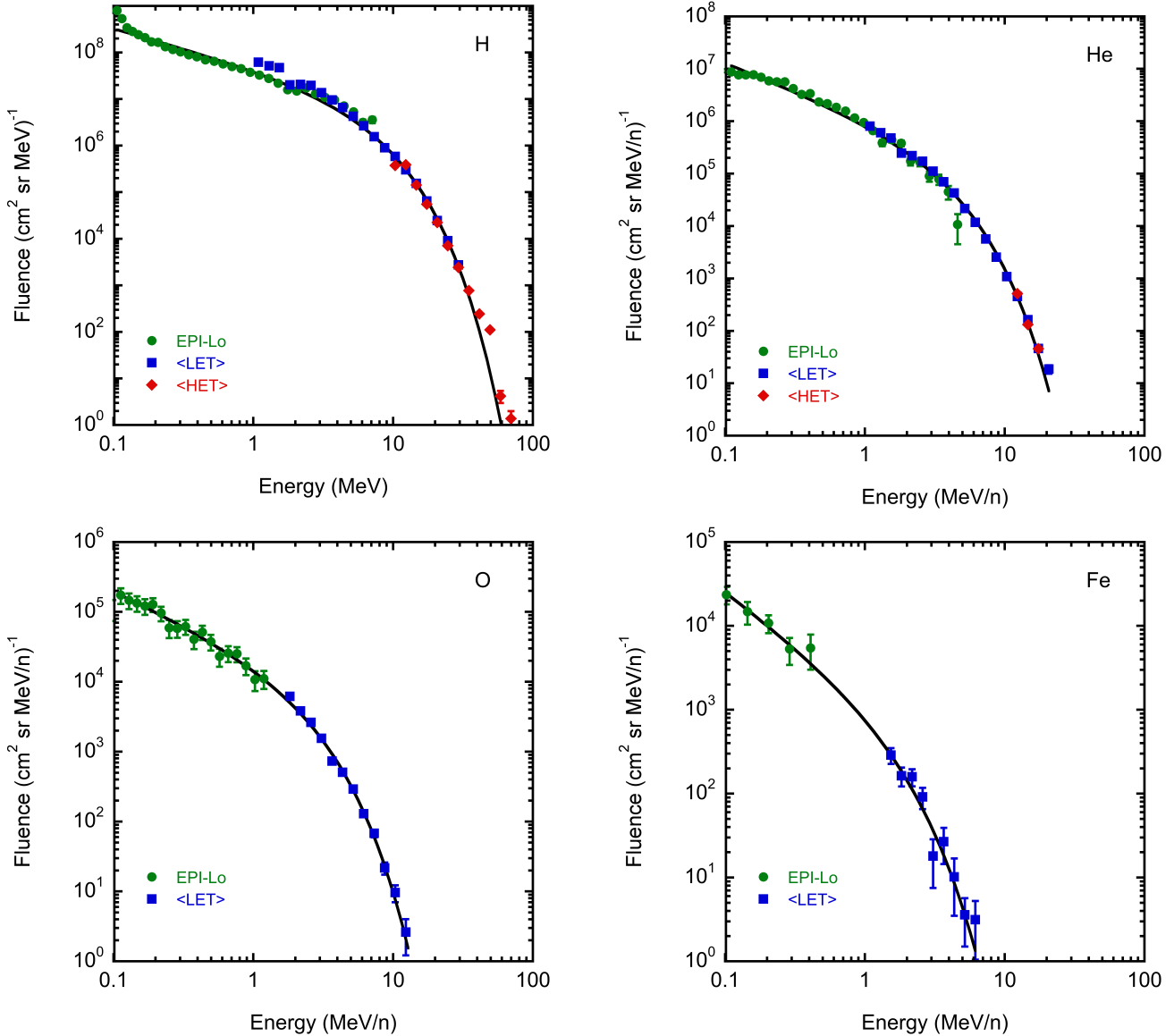


Fig. 8. Fluence spectra obtained during the decay of the SEP event (December 1 (day 336), 04:00 UT – December 4 (day 339), 17:00 UT) for H, He, O and Fe. H and He spectra combine data from EPI-Lo (green circles), the average of LETA and LETB (blue squares), and the average of HETA and HETB (red diamonds). O and Fe spectra do not have contributions from HET as the spectra did not extend into HET's energy range. The uncertainties shown are statistical; absolute intensities may be uncertain by as much as 30% (see text for details). The black curves are Ellison-Ramaty fits; parameters are given in Table 2.

a velocity-dispersed onset (with higher energy protons arriving before lower energy ones) is evident in the EPI-Lo data late on November 29 (day 334), consistent with that seen by LETA earlier in the day, clearly the shock was strong enough, or the surrounding turbulence high enough, to efficiently confine the majority of the lower energy particles to the vicinity of the shock and sheath region. This is consistent with the substantial intensity increase (historically referred to as an energetic storm particle, ESP, event) seen at the time of the shock passage (solid vertical line), which is discussed further in Sect. 6.

5. Spectra and composition

During the decay of the event, the particle distribution appears to be fairly isotropic with LETA and LETB exhibiting similar particle intensities (likewise for HETA and HETB). Thus for this portion of the event we use the average of LETA and LETB for a

combined ‘<LET>’ dataset and similarly for HETA and HETB to create a ‘<HET>’ dataset. The EPI-Lo data are averaged over the apertures¹ that most closely coincide with the fields of view of LETA and LETB and combined with measurements from <LET> of H, He, O and Fe and with <HET> for H and He to create fluence spectra for the decay portion of the event (December 1 (day 336), 04:00 UT – December 4 (day 339), 17:00 UT) in Fig. 8. The gap in the Fe spectrum from ~ 0.5 to ~ 1.3 MeV nuc $^{-1}$ is due to the different measurement techniques of EPI-Lo (time-of-flight) and EPI-Hi (dE/dx versus E). Additionally, the EPI-Lo energy bins for Fe have been combined to create fewer bins and increase the statistics within each bin. Full intercalibration between the sensors has not been completed and currently the <LET> spectra (for all species) are divided by a factor of 1.3 to be consistent with EPI-Lo and <HET>. This 30% difference may be

¹ Aperture numbers 21–30, 33–39, 44, 46, 48, 61–63, 70–73.

Table 2. Fit parameters ^(a) to the fluence spectra.

Element	K (cm ² sr MeV n ⁻¹) ⁻¹	γ	E_0 (MeV n ⁻¹)
H (decay)	$4.84 \pm 0.09 \times 10^7$	-0.84 ± 0.02	4.18 ± 0.05
He (decay)	$1.21 \pm 0.03 \times 10^6$	-1.04 ± 0.02	2.33 ± 0.09
O (decay)	$2.50 \pm 0.17 \times 10^4$	-0.92 ± 0.06	1.74 ± 0.04
Fe (decay)	$1.65 \pm 0.51 \times 10^3$	-1.22 ± 0.17	1.26 ± 0.27
O (full)	$2.34 \pm 0.07 \times 10^5$	-0.84 ± 0.03	2.79 ± 0.06
Fe (full)	$7.14 \pm 0.70 \times 10^4$	-0.72 ± 0.07	1.19 ± 0.06

Notes. ^(a)From a fit of the form $y = Kx^{-\gamma} \exp(-x/E_0)$, where y is fluence in (cm² sr MeV n⁻¹)⁻¹ and x is energy in MeV n⁻¹.

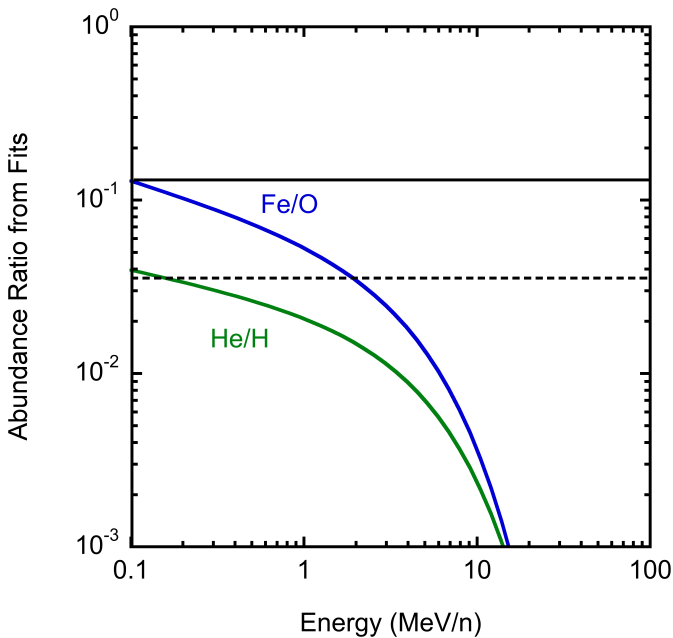


Fig. 9. Fe/O (blue curve) and He/H (green curve) abundance ratios versus energy as determined from the spectra fits. The average Fe/O ratio (at 5–12 MeV nuc⁻¹) and He/H ratio (at 1–4 MeV nuc⁻¹) reported by Reames (1999) are shown for reference as the solid and dashed horizontal lines, respectively.

related to remaining field of view differences, different obstructions in the sensors' fields of view, or to-be-improved energy or efficiency calibrations. Thus, the absolute fluence values presented here are uncertain by up to ∼30%.

All the spectra exhibit power laws at low energies with strong decreases in fluence at higher energies which are well fit by the form proposed by Ellison & Ramaty (1985) of a power law multiplied by an exponential. The parameters of the fits are listed in Table 2. As is often typical of SEP spectra associated with CME-driven shocks, the energy of the roll-over (E_0) is lower for the higher rigidity particles, for example, Fe, which is likely due to the lower efficiency of confining them to the shock region (Ellison & Ramaty 1985; Cohen et al. 2005; Tylka et al. 2005; Li et al. 2009). The values of E_0 obtained here are surprisingly low; values typical for large SEP events are above 10 MeV for protons (Tylka et al. 2000; Mewaldt et al. 2005). However, these spectra are from only the decay portion of the event and since intensities of higher energy ions generally decrease with time more rapidly than lower energies (see, e.g., Sollitt et al. 2008),

the higher energy particle contributions to the spectra are likely concentrated in the earlier portion of the event. Thus the comparison to spectra integrated over entire events (as is typical) may not be appropriate.

From the spectra fits, the composition as a function of energy can be determined and is presented as He/H and Fe/O abundance ratios in Fig. 9. The decreases with increasing energy seen in these ratios are consequences of the lower E_0 values for He relative to H and Fe relative to O. For comparison, the average He/H and Fe/O abundances as determined by Reames (1999) for large, shock-accelerated SEP events are indicated by horizontal lines. Clearly, the composition of the decay portion of the November 29 event below the roll-over energies is fairly typical.

The instrument response for electrons is complicated and requires careful modeling to extract fluence spectra. To date, this has only been completed for the HET telescope (Labrador et al., in prep.). The electron fluence spectrum during the decay of the SEP event from ⟨HET⟩ is given in Fig. 10a. It is consistent with a single power law in energy with a spectral index of −5.3. This is softer than the mean value of −3.6 for SEP electron spectra above a few hundred keV reported in a statistical survey of 45–425 keV electrons in SEP events by Dresing et al. (2020). However, unlike ours, those are full-event spectra.

In an initial attempt at calculating the full-event electron spectrum, we have removed the 4 min period when HET was in DT2 and calculated the sensor response during DT1 (as was done for DT0). The resulting fluence spectrum for the entire event (minus the 4 min of DT2) is presented in Fig. 10b. A fit to the spectrum yields a power law with index of −3.4; an additional fit to the lowest three energy points plus the two at ∼3 and ∼4 MeV is also shown. This steeper fit, with index −4.2, suggests an additional component dominating around 1.5–2.5 MeV and possibly a flattening of the spectrum above ∼4 MeV. Although not shown, the bump near 2 MeV is present in both HETA and HETB, while the flattening above 4 MeV is primarily evident in only HETB. The origin of these higher-energy components is not clear, but preliminary examination of the spectrum time evolution, indicates they are only present during the shock plus sheath period.

Due to the DT2 impact on the LET measurements of H and He, it is not similarly possible to create full-event spectra for all the ions. However, the effect of the raised thresholds during DT1 and DT2 on heavy ions was minor allowing combined ⟨LET⟩ and EPI-Lo spectra for O and Fe to be determined for the entire event. These (along with their fits) are compared to those of the decay portion of the event in Fig. 11. Naturally, the full event fluence is significantly higher than that of the decay portion alone, but the factor increase appears to be approximately twice as large for Fe than for O. This suggests that the Fe/O abundance, integrated over the full event, is larger than that derived for the decay, primarily below 1 MeV nuc⁻¹. Comparison of the spectral shapes shows that the O spectrum below ∼1 MeV nuc⁻¹ is approximately the same for the full event and the decay, however, the Fe spectrum is somewhat steeper at the low energies for the full event. In both spectra the ‘middle’ energies (i.e., between 1 and 10 MeV nuc⁻¹) ‘fill in’ in the full event spectra; for Fe this allows a better determination of the spectral roll-over. It should be noted, however, that the intercalibration of EPI-Lo and EPI-Hi for heavy ions, particularly during periods in which EPI-Hi is utilizing dynamic thresholds, has not been completed, leading to increased discrepancies between the two datasets for the full event spectra.

Overall the spectra and composition of the event are consistent with an SEP event dominated by acceleration at a CME-driven, quasi-parallel shock (see e.g., Tylka et al. 2005).

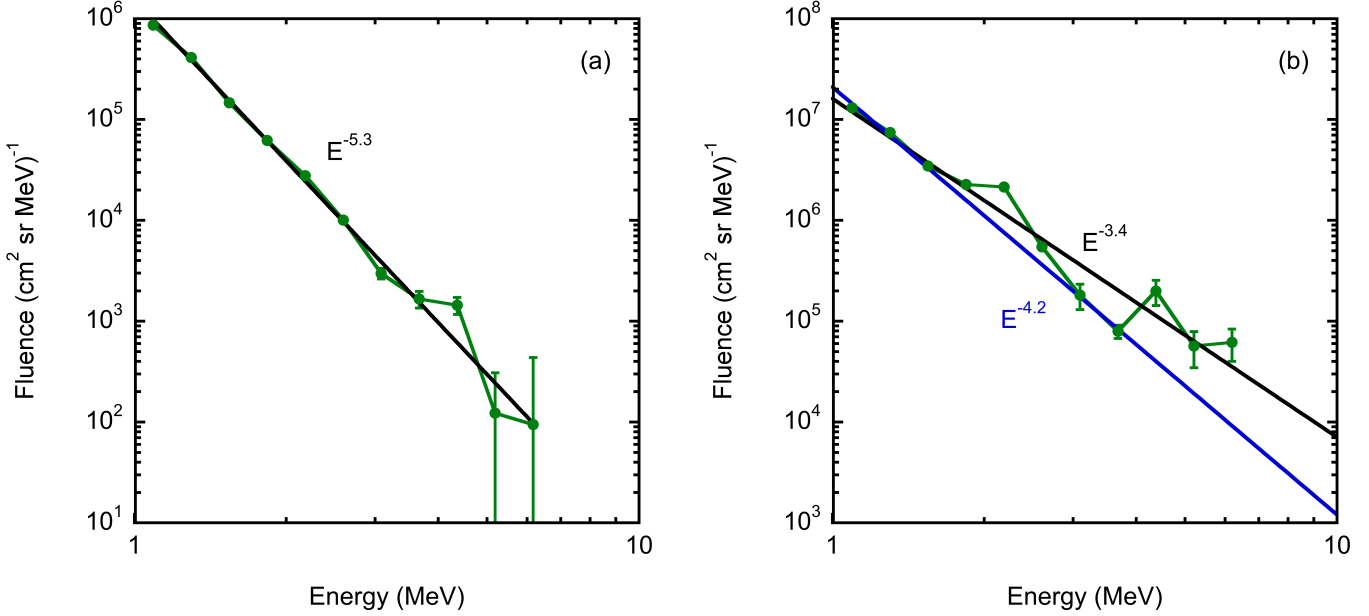


Fig. 10. Fluence spectrum of electrons from $\langle \text{HET} \rangle$ measured during the decay of the SEP event (*panel a*). The data are well fit by a power law with a spectral index of -5.3 . The electron spectrum for the full event (excluding a 4 min period of DT2) is shown in *panel b* with two power law fits of indices -3.4 and -4.2 (see text for details).

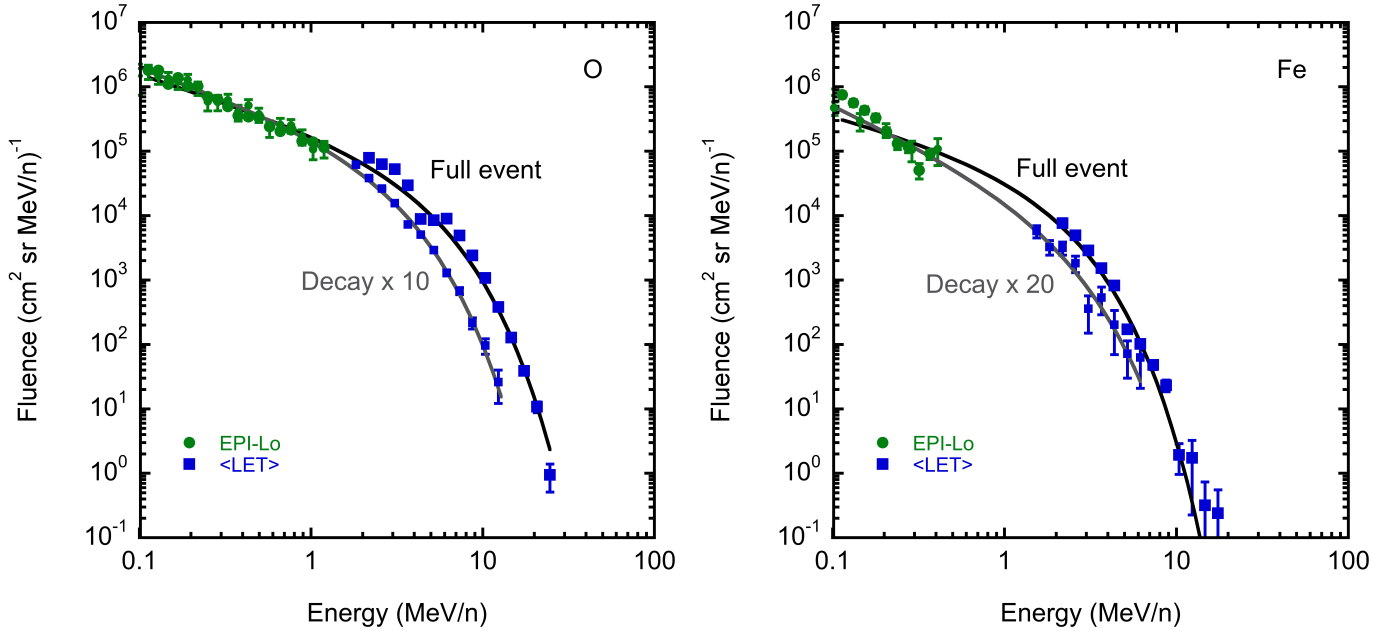


Fig. 11. Comparison of the fluence spectra obtained for the full event (large symbols) and the decay (small symbols; also shown in Fig. 8) for O and Fe from EPI-Lo (green circles) and the average of LETA and LETB (blue squares). The decay spectra have been scaled (as indicated) to provide agreement near ~ 0.3 MeV n⁻¹. The fit parameters are listed in Table 2.

As we lack in-situ observations near the Sun, we cannot verify the shock properties where many of the higher energy particles are likely accelerated. Unfortunately, due to the spacecraft orientation, accurate solar wind parameters are not available during the shock period, making it also difficult to determine the local shock properties as it passes over PSP. Ongoing studies suggest the region is also complicated by the interaction of the slower November 26 CME and the fast November 29 CME at this time. As discussed in Nieves-Chinchilla et al. (2021), this interaction may even contribute to the formation of the shock observed by PSP on November 30. Their initial calculations

indicate that the shock is quasi-parallel, but relatively newly formed.

Given the speed of the November 29 CME (~ 1700 km s⁻¹), the location of the active region (approximately central meridian as viewed by PSP), and the observation of a type II radio burst (see Fig. 13) suggesting the presence of an interplanetary shock (Gopalswamy et al. 2008), one might have expected a stronger SEP event (such as November 4, 2001 or July 14, 2000 Tylka et al. 2005, and references therein) with higher E_0 values in the ion spectra. However, the CME was traveling significantly southeastward and PSP was nominally connected to

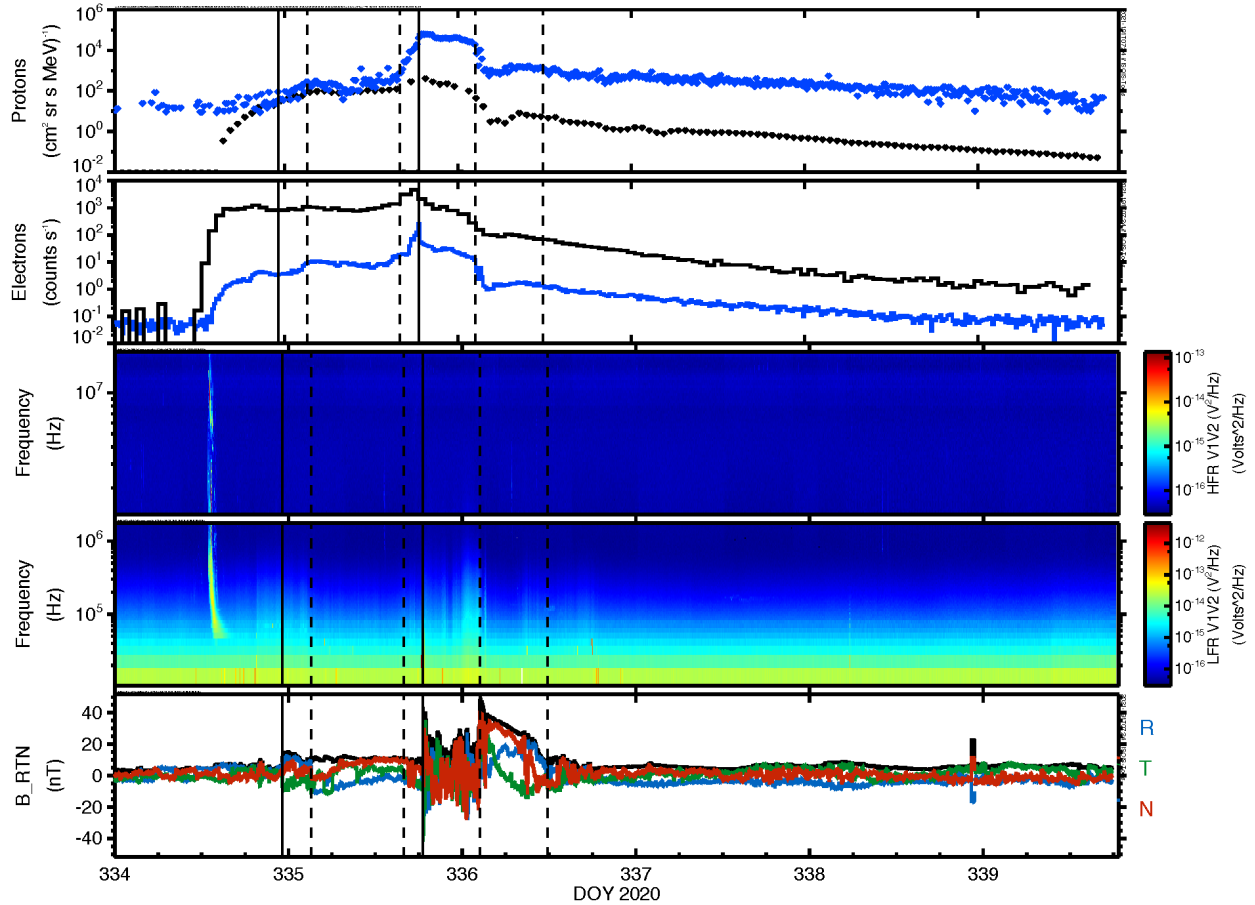


Fig. 12. Overview of the SEP event showing proton intensities at 0.5 and 10 MeV (top panel, blue and black traces, respectively), electron rates at 150 keV and 1 MeV (second panel, blue and black traces respectively), and the radio and magnetic field data (bottom three panels). The time of the shock passages are marked by the solid vertical lines and the periods of the magnetic clouds are bounded by the pairs of dashed vertical lines.

the western flank of the CME at the start of the event, which was moving much more slowly than the southeast flank. Additionally, the CME experienced significant deceleration as it traveled away from the Sun (Kollhoff et al. 2021, Fig. 3), suggesting the shock related to the type II burst may have been short lived. Thus, the relative lack of high energy particles may be due to PSP being connected to a weak acceleration region during the early portion of the event, when typically the higher energy particles are generated. Closer examination of the details of the CME evolution and modeling of the magnetic connection between PSP and the shock are needed to fully understand the particle signatures. Among the modeling efforts underway is one that employs the SPE Threat Assessment Tool (STAT, Linker et al. 2019; Young et al. 2021). STAT utilizes coupled magnetohydrodynamic and focus transport equations to simulate the full eruption of the CME and the acceleration and transport of the SEPs through the inner heliosphere. Application of this tool to the November 29 event will allow the parameters of the CME shock near the Sun and their effects on the SEPs to be explored (Caplan et al., in prep.).

6. Temporal evolution

The temporal evolution of the proton intensities at 0.5 and 10 MeV (from EPI-Lo and ⟨HET⟩, respectively) and electron count rates at 150 keV (EPI-Lo) and 1 MeV (⟨HET⟩) are presented, along with the radio and magnetic field data, in Fig. 12. The small shock associated with the November 26 CME is

detected by PSP on November 29 (day 334) at 23:07 UT and followed by a magnetic cloud on November 30 from 03:07–15:56 UT (indicated by the solid line and pair of dashed lines, respectively). The passage of the larger shock from the November 29 CME occurs on November 30 (day 335), 18:35 UT (the second solid line), followed by a large sheath region. The associated magnetic cloud is evident by the rotation in the B_R and B_T components, starting at December 1 (day 336), 02:24 UT and ending at 11:45 UT (dashed lines). Due to the lack of solar wind parameters during this period, these structures are identified using the magnetic field data only. The initial type III radio burst occurs during the rise of the soft X-rays at 12:54 UT and continues through the peak of the flare at 13:11 UT, along with a type II radio burst (best seen in Fig. 13). Although comparison of the onset of the 1 MeV electron count rate and the type III burst give the indication that the onset occurs before the radio burst, this is an artifact of the 1-h time resolution plotted. An examination of higher time-resolution data (but lower energy resolution) indicates the electron onset is ∼13:28 UT, or ∼34 min after the first type III.

As is clear in the spectrograms of Fig. 6, the 0.5 MeV protons are fairly well contained to the strong shock region, exhibiting a classic ESP signature (see, e.g., Cohen 2006, and references therein). The particle intensities increase quickly as the shock approaches the spacecraft and reach a maximum at the time of the shock’s passage, due to particles being locally accelerated. The ESP event extends to ∼1 MeV in energy, above which an intensity peak near the shock is difficult to discern. The analysis

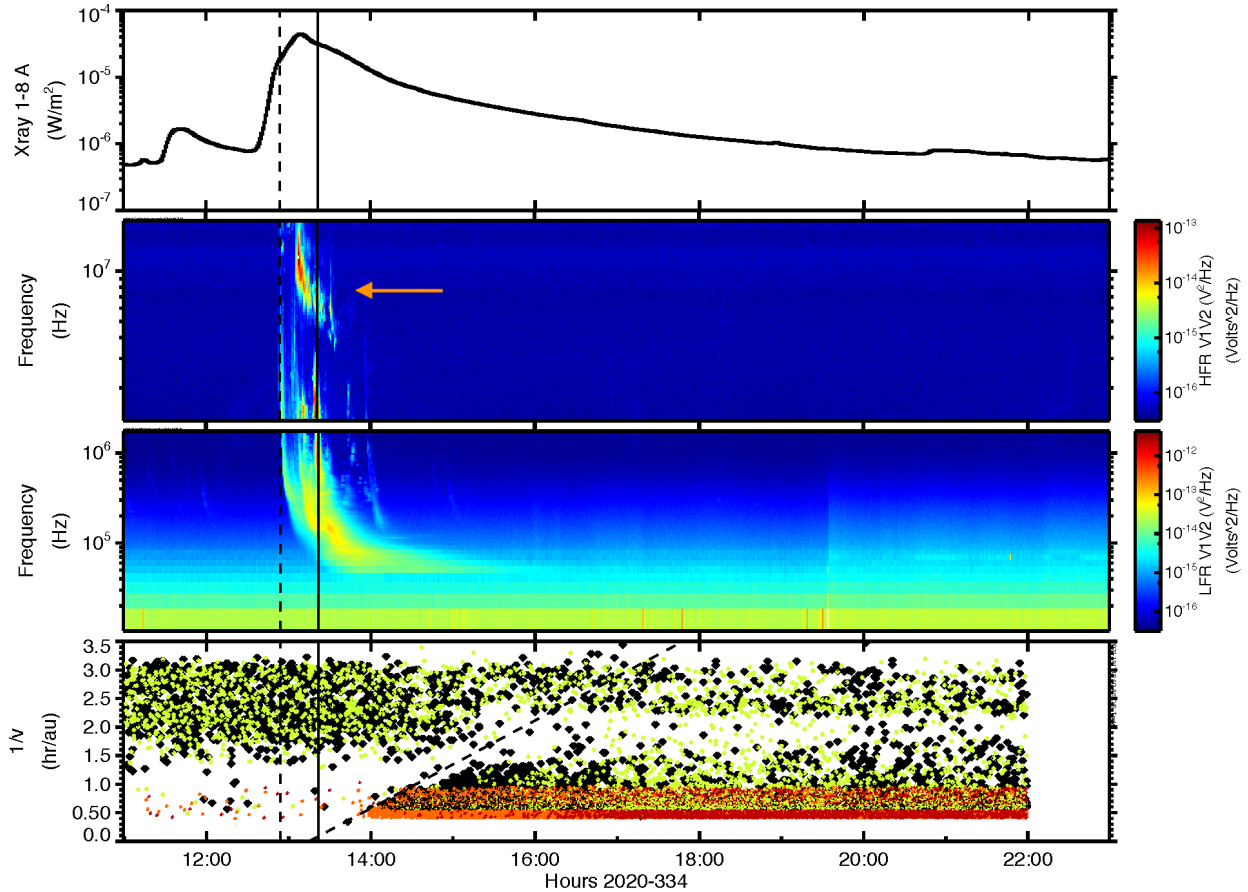


Fig. 13. Onset of the event showing the soft X-ray data from GOES-16 (*top panel*), the PSP radio high and low frequency observations (*middle panels*) and the inverse velocity of individual ions measured by LETA (black symbols), LETB (green symbols), HETA (orange symbols) and HETB (red symbols). The onset of the event is apparent as an ‘edge’ to the inverse velocity data points, fit by eye (over the range of $\sim 0.5\text{--}1.25\text{ h au}^{-1}$), and delineated by the dashed line. The x -intercept of this line corresponds to the release time of the particles at the Sun. This time, shifted by 6.67 min, is shown by the solid vertical line for comparisons with the X-ray and radio data. The start of the multiple type III radio bursts is marked by the dashed vertical line and a type II burst is indicated by the orange arrow.

of the magnetic field data indicating a quasi-parallel shock is consistent with the ESP signature (Nieves-Chinchilla et al. 2021). The details of this shock and corresponding ESP event are also described and discussed in Giacalone et al. (2021).

Interestingly, the electron count rates at both 150 keV and 1 MeV also peak at the time of the strong shock. It is rare to see local shock acceleration of electrons; one recent study found only 1% of interplanetary shocks had associated electron ESP events (Dresing et al. 2016) and several modeling efforts have indicated that it is difficult to accelerate electrons to energies >100 keV at quasi-parallel shocks (see e.g., Trotta & Burgess 2019; Guo & Giacalone 2015, and references therein). A possible explanation is that the electrons are not being locally accelerated but are somehow trapped in the vicinity of the shock. Such a trap may have been created by the combination of the two CMEs, bounding a region which contained particles effectively (particularly electrons with their small gyroradii) and became increasingly narrow as the fast CME caught up to the preceding slow one. A similar trapping scenario was proposed as the source of a second injection of MeV electrons in a wide-longitude SEP electron event examined by Dresing et al. (2018). This might also be related to the additional 2 MeV and >4 MeV components of the electron spectrum seen in Fig. 10b, but more detailed study is needed.

Figure 13 presents a closer examination of the onset of the event. The top panel shows the soft X-ray emission measured by

GOES-16; the middle panels show the complexity of the type III emission as observed by PSP, with several individual bursts, as well as the type II at the higher frequencies starting close to the time the X-ray emission peaks. The bottom panel shows the inverse velocities of individual ions measured by LETA, LETB, HETA and HETB as a function of the time they were observed. The onset of the event is evident as the increase in the density of data points along a sloped line. Fitting this edge by eye over the $1/v$ range of $\sim 0.5\text{--}1.25\text{ h au}^{-1}$, yields a release time at the Sun (the x -intercept) of 13:15 UT and a path length of 1.3 au (the inverse slope of the line). The vertical line on the plot is this release time shifted forward by 6.67 min to allow comparison to the electromagnetic emissions in the upper panels.

The derived time suggests that the particles were released shortly after the X-ray peak emission, towards the end of the series of type III bursts and when the type II emission had drifted down to ~ 6 MHz. Based on the time-height profile of the CME, the CME was $<5 R_\oplus$ at this time. Although there is some uncertainty in the derivation of the release time (~ 5 min) as well as general concerns over the methodology (Sáiz et al. 2005; Agueda et al. 2014; Vainio et al. 2013), many SEP studies have reported similarly low CME heights (Reames 2009), although usually for SEP events with hard ion spectra extending to hundreds of MeV. Detailed discussion on how this release time compares to that derived from SEPs observed at other spacecraft

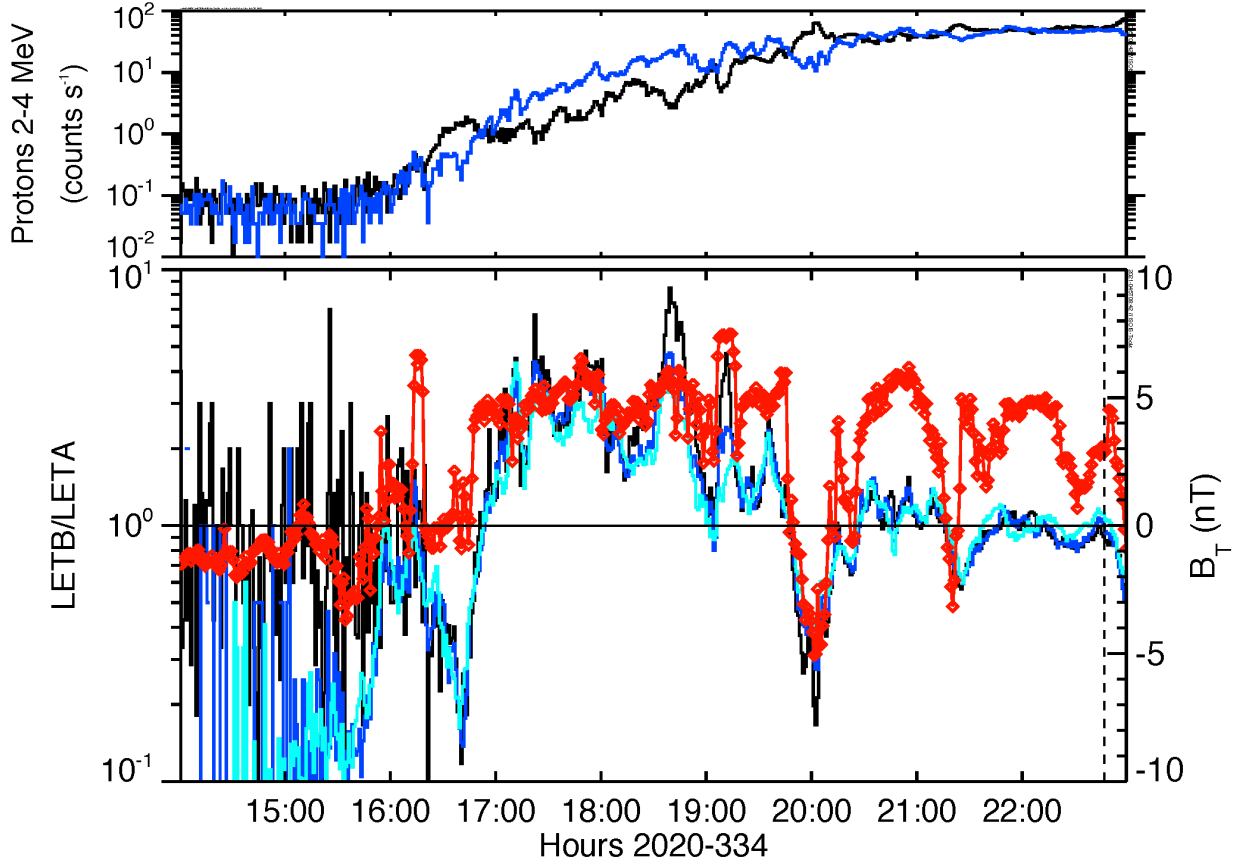


Fig. 14. Onset of the event as observed in 1-min LET proton sectored rates, summed to correspond to LETB (blue, viewing particles traveling in the +T direction) and LETA (black, viewing particles traveling in the -T direction), for 2–4 MeV (upper panel). The ratio of these rates for the 2–4 MeV (black), 4–8 MeV (blue), and 8–16 MeV (cyan) protons indicates whether particles are predominantly flowing in the +T direction (values >1) or the -T direction (values <1). For comparison, the T component of the magnetic field is given in red symbols (right axis). The dashed vertical line indicates when the spacecraft rolled 180° resulting in LETA viewing the +T-flowing protons and LETB viewing -T-flowing protons.

(e.g., STEREO-A and Solo) and corresponds to solar activity, such as the observed EUV wave, can be found in Kollhoff et al. (2021). Future work, modeling of the CME and shock, along with the magnetic field line connection to PSP, will enable the location of the shock and its properties to be determined at the time of the particle release.

The derived pathlength of 1.3 au is significantly longer than the nominal Parker spiral length of 0.98 au (Kollhoff et al. 2021). Such increased pathlengths have been observed in other SEP events measured by ISOIS (Cohen et al. 2021). A possible explanation discussed by Chhiber et al. (2021) is that field line random walk, as well as gyroradius effects, results in the long pathlength experienced by the particles and is reflected in their velocity-dispersed arrival times. For an observer at 0.8 au, their calculations suggest a pathlength of \sim 1.4 au (before consideration of gyroradii effects, see Fig. 6 of their paper), quite similar to our derived value of 1.3 au. Similar considerations have also been examined by Laitinen & Dalla (2019). They find that the pathlength can depend strongly on the longitude of the source region relative to the observer, with pathlengths being as much as twice the length of the nominal Parker spiral.

Although LETA was not viewing along the nominal Parker spiral due to the spacecraft rotation at the time of the event, there are still some interesting anisotropic features apparent in the data during the onset. LETA was looking along the +T direction (in RTN coordinates) and LETB along the -T direction at the start

of the event. Unfortunately, the high energy-resolution data are only available on an hourly cadence due to telemetry limitations. However, there are 1-min sectored proton rates, accumulated in broad energy bins (2–4, 4–8, 8–16 MeV), which can be summed to roughly correspond to protons traveling in the +T and -T directions (i.e., as would be measured by LETB and LETA, respectively). It can be seen in the top panel of Fig. 14 that initially there are approximately equal numbers of protons traveling in both directions, but this is followed by periods where one direction dominates over the other. The ratio of the rates of +T-traveling to -T-traveling particles (i.e., LETB/LETA) is shown in the lower panel (for all three energy bins) along with the value of the T component of the magnetic field. Here it is clear that when B_T is positive, the +T-traveling proton rate is higher and vice versa. This indicates that the particles are predominantly flowing along the direction of the magnetic field, despite switches in the field direction as observed by the spacecraft. Careful examination reveals a time period near the end of the plot where this correlation appears to change sign. However, this is after the spacecraft had rolled 180° (as indicated by the vertical line) causing the sectors previously identified as measuring particles flowing in the +T or -T direction to be reversed. Thus, the signal is still consistent with particles flowing along the direction of the magnetic field.

Another, higher time resolution data product available from HET is the rate of protons stopping in various detectors of

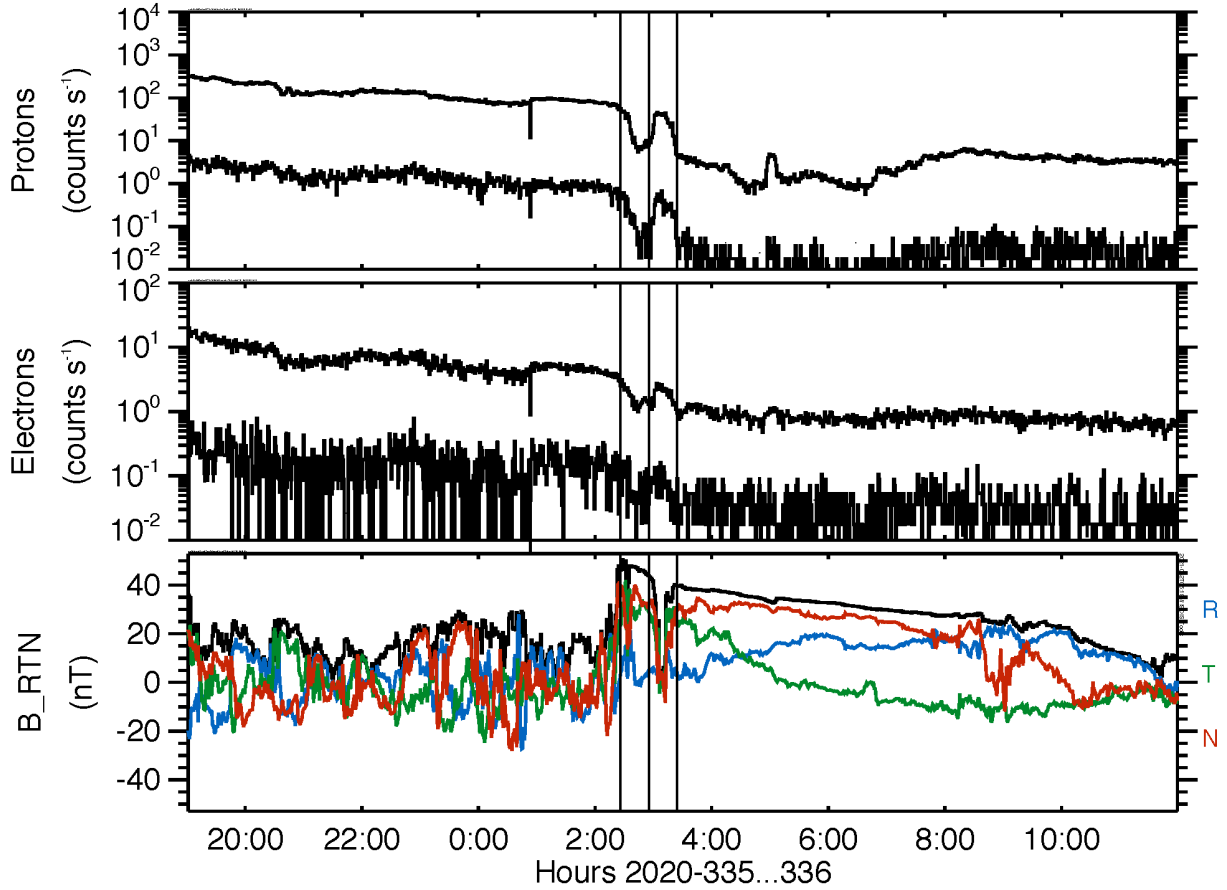


Fig. 15. Sheath and cloud portion of the event as measured in 1-min rates of protons stopping in the third and fifth detector of HET (upper and lower traces, respectively, of the *top panel*) and electrons stopping in the third and fourth HET detectors (upper and lower traces, respectively, of the *second panel*). *Bottom panel*: magnitude and components of the magnetic field. Vertical lines indicate features seen in the particle rates that correspond to changes in the magnetic field. See text for details.

the telescope (in this rate, HETA and HETB are combined). Although converting these rates into intensities is difficult because the particles stopping in a given detector span a wide range of energies, the temporal variation in the count rate still provides useful information. The rate of protons stopping in the third and fifth detectors of HET (referred to as R2 and R4, respectively) correspond roughly to energies of 15–25 MeV and 30–40 MeV and are shown for the sheath plus cloud portion of the event in Fig. 15. Also included are two electrons rates from HET; these also have a broad energy response and are even more complicated due to scattering in the instrument, but the responses peak around ~ 2 and ~ 3 MeV (see Fig. 6 of Wiedenbeck et al. 2017).

Shortly after the onset of the magnetic cloud, the particle intensities drop dramatically. This is not uncommon and considered a result of the particles being unable to penetrate the magnetic cloud structure (see, e.g., Blanco et al. 2013; Malandraki et al. 2003, and references therein). What is unusual is the brief increase in particle intensities on December 1 (day 336) between 02:55 UT and 03:25 UT. This is apparent in both the proton and electron rates and is coincident with an abrupt, short-lived, change in the magnetic field direction and magnitude. One interpretation is that PSP briefly exited the cloud, entered a region filled with SEPs, and then returned to the cloud.

There is a second, smaller, temporary increase in the R2 proton rate a couple of hours later. This is not accompanied by a change in the magnetic field (or clearly seen in the electron

rates). This could be a similar event, but one where PSP does not quite exit the cloud but is close enough to the edge to observe particles outside the cloud with sufficiently large gyroradii to cross the cloud boundary for a short distance. As electrons have much smaller gyroradii, this is consistent with the lack of signal in the electron rates.

7. Summary

On 29 November 2020, PSP observed its first mid-sized SEP event during the early increase in solar activity of cycle 25. The energetic particle suite, IS \odot IS, performed well with only a few minor issues, providing an opportunity to calibrate the heavy ion response of many of the sensors for the first time since launch. The ion spectra both during the decay of the event (where the data are the most complete for H and He) and integrated over the full event (possible for O and Fe) are well described by a power law multiplied by an exponential with roll-over energies that decrease with the species' increasing rigidities. This, along with the He/H and Fe/O composition ratios, is fairly typical of SEP events where the dominant source is acceleration at a CME-driven shock. The electron spectrum during the decay of the event is a power law with an index that is substantially softer than usual for SEP events, but the power-law index for the full event is nominal. Interestingly, the full-event spectrum suggests contributions from higher-energy components (Fig. 10b), primarily present during the shock and sheath periods. This may

be a population trapped between the event CME and a preceding, slower CME.

Due to the relative positions of PSP and the solar source region, the CME passed over the spacecraft. At this time, it was also overtaking a previous slower CME; this may have contributed to the complicated shock and large sheath region observed by PSP. At the time of the shock, a local population of ions with energies up to at least ~ 1 MeV was observed (possibly locally accelerated), along with an increase in the count rate of 0.5 and 1 MeV electrons (most likely trapped by the CME-CME interaction). The turbulent sheath region was followed by a magnetic rotation consistent with a flux rope structure, or magnetic cloud. During the cloud passage, the SEP intensities dropped significantly with a brief return to high intensities as PSP temporarily passed out of the cloud region.

The onset of the event exhibited some anisotropy with the particles predominantly flowing along the direction of the magnetic field, following magnetic field changes in orientation as viewed by the spacecraft. Velocity dispersion analysis of the first arriving ions indicates a solar release time of 13:15 UT on November 29 (day 334), when the CME was within $5 R_S$ of the Sun and coincident with type II emission indicating the presence of a shock.

The SEP event was also observed by several spacecraft positioned at widely separated longitudes around the Sun, including SolO, STEREO-A, and near-Earth spacecraft such as ACE, Wind and SOHO. This makes it a noteworthy circumsolar event, generating interest internationally from multi-spacecraft member teams; initial multi-spacecraft results are presented in Kollhoff et al. (2021). Further understanding of the particulars of the CME eruption, and subsequent particle acceleration and transport will result from upcoming modeling efforts and more detailed SEP analysis. The observations by IS \odot IS during this event show that the suite is well positioned to observe future SEP events as PSP continues to travel closer to the Sun and the solar activity continues to increase in cycle 25.

Acknowledgements. This work was supported by NASA's Parker Solar Probe Mission, contract NNN06AA01C. Parker Solar Probe was designed, built, and is now operated by the Johns Hopkins Applied Physics Laboratory as part of NASA's Living with a Star (LWS) program. Support from the LWS management and technical team has played a critical role in the success of the Parker Solar Probe mission. We thank all the scientists and engineers who have worked hard to make PSP a successful mission. In particular, we thank B. Kecman, W. R. Cook and J. Burnham, without whom the EPI-Hi instrument would not be possible. C. M. S. Cohen thanks T. Nieves-Chinchilla and A. Szabo for their helpful discussions regarding the shock and ICME observations, and N. Dresing for useful ones on electron ESP events. S. D. Bale acknowledges support of the Leverhulme Trust Visiting Professorship program. A. Vourlidas acknowledges support from NASA grants 80NSSC19K1261 and 80NSSC19K0069. The Sun Earth Connection Coronal and Heliospheric Investigation (SECCHI) was produced by an international consortium of the Naval Research Laboratory (USA), Lockheed Martin Solar and Astrophysics Lab. (USA), NASA Goddard Space Flight Center (USA), Rutherford Appleton Laboratory (UK), University of Birmingham (UK), Max Planck Institute for Solar System Research (Germany), Centre Spatial de Liège (Belgium), Institut d'Optique Théorique et Appliquée (France), and Institut d'Astrophysique Spatiale (France). STEREO/SECCHI data are available for download at <https://secchi.nrl.navy.mil/>. This paper uses data from the CACTus CME catalog, generated and maintained by the SIDC at the Royal Observatory of Belgium. The IS \odot IS data and visualization tools

are available to the community at <https://spacephysics.princeton.edu/missions-instruments/isois>; data are also available via the NASA Space Physics Data Facility (<https://spdf.gsfc.nasa.gov/>). The GOES X-ray data are available from the National Centers for Environmental Information (<https://www.ngdc.noaa.gov/stp/spaceweather.html>).

References

- Agueda, N., Klein, K.-L., Vilmer, N., et al. 2014, *A&A*, **570**, A5
 Bale, S. D., Goetz, K., Harvey, P. R., et al. 2016, *Space Sci. Rev.*, **204**, 49
 Blanco, J. J., Hidalgo, M. A., Gómez-Herrero, R., et al. 2013, *A&A*, **556**, A146
 Chhiber, R., Matthaeus, W. H., Cohen, C. M. S., et al. 2021, *A&A*, **650**, A26
 Cohen, C. M. S. 2006, *Sol. Erupt. Energ. Part.*, **165**, 275
 Cohen, C. M. S., Stone, E. C., Mewaldt, R. A., et al. 2005, *J. Geophys. Res.*, **110**, A09S16
 Cohen, C. M. S., Mason, G. M., & Mewaldt, R. A. 2017, *ApJ*, **843**, 132
 Cohen, C. M. S., Christian, E. R., Cummings, A. C., et al. 2021, *A&A*, **650**, A23
 Dresing, N., Theesen, S., Klassen, A., & Heber, B. 2016, *A&A*, **588**, A17
 Dresing, N., Gómez-Herrero, R., Heber, B., et al. 2018, *A&A*, **613**, A21
 Dresing, N., Effenberger, F., Gómez-Herrero, R., et al. 2020, *ApJ*, **889**, 143
 Ellison, D. C., & Ramaty, R. 1985, *ApJ*, **298**, 400
 Fox, N. J., Velli, M. C., Bale, S. D., et al. 2016, *Space Sci. Rev.*, **204**, 7
 Giacalone, J., Mitchell, D. G., Allen, R. C., et al. 2020, *ApJS*, **246**, 29
 Giacalone, J., Burgess, D., Bale, S. D., et al. 2021, *ApJ*, submitted
 Gopalswamy, N., Yashiro, S., Akiyama, S., et al. 2008, *Ann. Geophys.*, **26**, 3033
 Guo, F., & Giacalone, J. 2015, *ApJ*, **802**, 1
 Hill, M. E., Mitchell, D. G., Andrews, G. B., et al. 2017, *J. Geophys. Res.: Space Phys.*, **122**, 1513
 Hill, M. E., Mitchell, D. G., Allen, R. C., et al. 2020, *ApJS*, **246**, 65
 Joyce, C. J., McComas, D. J., Schwadron, N. A., et al. 2021, *A&A*, **651**, A2
 Kasper, J. C., Abiad, R., Austin, G., et al. 2016, *Space Sci. Rev.*, **204**, 131
 Kollhoff, A., Kouloumvakos, A., Lario, D., et al. 2021, *A&A*, **656**, A20 (SO Cruise Phase SI)
 Laitinen, T., & Dalla, S. 2019, *ApJ*, **887**, 222
 Lario, D., Richardson, I. G., Palmerio, E., et al. 2021, *ApJ*, submitted
 Leske, R. A., Christian, E. R., Cohen, C. M. S., et al. 2020, *ApJS*, **246**, 35
 Li, G., Zank, G. P., Verkhoglyadova, O., et al. 2009, *ApJ*, **702**, 998
 Linker, J., Caplan, R. M., Schwadron, N. A., et al. 2019, *J. Phys. Conf. Ser.*, **1225**, 012007
 Malandraki, O. E., Sarris, E. T., & Tsiropoula, G. 2003, *Ann. Geophys.*, **21**, 1249
 McComas, D. J., Alexander, N., Angold, N., et al. 2016, *Space Sci. Rev.*, **204**, 187
 McComas, D. J., Christian, E. R., Cohen, C. M. S., et al. 2019, *Nature*, **576**, 223
 Mewaldt, R. A., Cohen, C. M. S., Labrador, A. W., et al. 2005, *J. Geophys. Res.*, **110**, A09S18
 Mitchell, D. G., Giacalone, J., Allen, R. C., et al. 2020, *ApJS*, **246**, 59
 Müller, D., Nicula, B., Felix, S., et al. 2017, *A&A*, **606**, A10
 Müller, D., St Cyr, O. C., Zouganelis, I., et al. 2020, *A&A*, **642**, A1
 Nieves-Chinchilla, T., Alzate, N., Cremades, H., et al. 2021, *ApJ*, submitted
 Patsourakos, S., Vourlidas, A., & Stenborg, G. 2013, *ApJ*, **764**, 125
 Pulupa, M., Bale, S. D., Bonnell, J. W., et al. 2017, *J. Geophys. Res.*, **122**, 2836
 Reames, D. V. 1999, *Space Sci. Rev.*, **90**, 413
 Reames, D. V. 2009, *ApJ*, **693**, 812
 Sáiz, A., Evenson, P., Ruffolo, D., & Bieber, J. W. 2005, *ApJ*, **626**, 1131
 Schwadron, N. A., Bale, S., Bonnell, J., et al. 2020, *ApJS*, **246**, 33
 Sollitt, L. S., Stone, E. C., Mewaldt, R. A., et al. 2008, *ApJ*, **679**, 910
 Sun, X., & Norton, A. A. 2017, *Res. Notes Am. Astron. Soc.*, **1**, 24
 Trotta, D., & Burgess, D. 2019, *MNRAS*, **482**, 1154
 Tylka, A. J., Boberg, P. R., McGuire, R. E., Ng, C. K., & Reames, D. V. 2000, *AIP Conf. Proc.*, **528**, 147
 Tylka, A. J., Cohen, C. M. S., Dietrich, W. F., et al. 2005, *ApJ*, **625**, 474
 Vainio, R., Valtonen, E., Heber, B., et al. 2013, *J. Space Weather Space Clim.*, **3**, A12
 Wiedenbeck, M. E., Angold, N. G., Birdwell, B., et al. 2017, *Int. Cosm. Ray Conf.*, **35**, 16
 Wiedenbeck, M. E., Bucik, R., Mason, G. M., et al. 2020, *ApJS*, **246**, 42
 Young, M. A., Schwadron, N. A., Gorby, M., et al. 2021, *ApJ*, **909**, 13